Catalysis
Science &
Technology

ROYAL SOCIETY
OF CHEMISTRY

PAPER

Cite this: *Catal. Sci. Technol.*, 2016, **6**, 1930

Phosphorus-doped ordered mesoporous carbons embedded with Pd/Fe bimetal nanoparticles for the dechlorination of 2,4-dichlorophenol†

Yaoyu Zhou,[ab] Lin Tang,*[ab] Guide Yang,[ab] Guangming Zeng,*[ab] Yaocheng Deng,[ab] Bingbing Huang,[ab] Ye Cai,[ab] Jing Tang,[ab] Jingjing Wang[ab] and Yanan Wu[ab]

Received 9th September 2015,
Accepted 28th October 2015

DOI: 10.1039/c5cy01514f

www.rsc.org/catalysis

Palladium/iron (Pd/Fe) bimetallic nanoparticles were embedded within phosphorus-doped ordered mesoporous carbons (Pd/NZVI@P) with high dechlorination activity for 2,4-dichlorophenol (2,4-DCP). The Pd/Fe bimetal nanoparticles of about 15 nm diameter embedded in phosphorus-doped ordered mesoporous carbons (P-OMCs) were homogeneously distributed. The high dechlorination activity was mainly attributed to the homogeneous distribution of Pd/Fe bimetal nanoparticles, which were characterized by transmission electron microscopy (TEM) and scanning electron microscopy/energy dispersive X-ray spectrometry (SEM/EDS) with image mapping. Dechlorination kinetics indicated that the dechlorination rates of 2,4-DCP increased with the increasing of Pd content. The use of P-OMCs as supporting materials to embed enough Pd/Fe bimetal nanoparticles kept the nanoparticles highly active and stable. Besides, solution pH had a significant effect on the dechlorination of 2,4-DCP and the passivation of the Pd/NZVI@P samples. The effects of the number and position of chlorine atoms for different chlorophenols (CPs) on the dechlorination activity were also revealed; the result indicated that the dechlorination of CPs by catalytic reduction preferentially begins from the *para*-position of the ring, and more chlorine atoms of CPs are favorable for the occurrence of the dechlorination reaction. This study demonstrated that P-OMC is a promising supporting material for the preparation of some effective composite metals for the catalytic dechlorination of CPs.

Introduction

Chlorophenols (CPs) are important chemical raw materials and intermediates and are known to be very toxic even at low concentrations.[1,2] Recently, the synthesis and use of bimetallic materials to work efficiently for the dechlorination of chlorophenol (CP) contaminants have been documented.[3–7] In these bimetallic materials, the first metal (such as Fe, Mg, Al, Zn, Sn, Si) with a low standard redox potential is oxidized more rapidly when coupled with the second metal (Cu, Ni, Ag, or Pd) with a high standard redox potential.[7] Among them, Pd/Fe is the most investigated bimetallic material because of the excellent hydrogenation activity of Pd and the low cost of Fe.[5,8] The high reactivity of nanoscale Fe/Pd bimetallic material seems promising in the liquid phase treatment of CPs, with many reports focusing on the reaction mechanisms, contaminant degradation kinetics, and reaction products.

However, some scientific and technical challenges remain in the degradation of chlorophenols (CPs) using Pd/Fe bimetallic materials. For example, Pd/Fe bimetallic materials have extremely low solubility in water (at most, 4–5 mg L^{-1}),[9,10] and nanoscale Pd and Fe particles are thermodynamically unstable in solution and tend to aggregate into larger particles.[11,12] Consequently, a stabilizer or a supporting template is often required to acquire stable and discrete Pd and Fe particles. To achieve these goals, nanostructured porous carbon materials, such as zeolite,[13] mesoporous silica,[14] active carbon,[15] mesoporous carbon and multi-walled carbon nanotubes,[16] have been developed as popular catalytic supports. Among them, ordered mesoporous carbon (OMC) has obtained great attention since it was discovered in 1999.[17]

Recently, more and more OMC materials were introduced as catalyst supports by researchers for the following reasons: (1) their large surface area and accessible porosity are indispensable when acquiring highly dispersed metal nanoparticles on the active nucleation sites of OMC, such as Pt/carbon,[18] PtCu/carbon,[19] Pd/carbon[20] and PtRu/carbon;[21] (2) the surface and physicochemical properties of OMC can be easily modified with functional groups or incorporated with

---

[a] *College of Environmental Science and Engineering, Hunan University, Changsha, 410082, China. E-mail: tanglin@hnu.edu.cn, zgming@hnu.edu.cn; Fax: +86 731 88822778; Tel: +86 731 88822778*

[b] *Key Laboratory of Environmental Biology and Pollution Control (Hunan University), Ministry of Education, Changsha 410082, Hunan, PR China*

† Electronic supplementary information (ESI) available: More details about the preparation of SBA-15 templates, 2,4-dichlorophenol analysis and thermogravimetric-differential thermal analysis. See DOI: 10.1039/c5cy01514f

heteroatoms (N, B, and S), exhibiting improved physical or chemical properties. Different from the traditional carbons (including carbon black, activated carbon, carbon nanofibers, and carbon nanotubes) poor in functional groups, its impregnation of noble metal will not result in aggregation or leaching of the particles in the liquid solution because of the strong interaction between the noble metal and the OMC support. For example, Yu and co-workers reported ordered uniform porous carbon networks with high surface area and well-developed porosity which were applied to support Pt(50)–Ru(50), and exhibited much higher specific activity for methanol oxidation than the vulcan carbon-supported catalyst by about 15%.[22] In our previous studies, magnetic mesoporous carbon incorporated with polyaniline,[23] iron-doped ordered mesoporous carbon[24] and nitrogen-functionalized magnetic ordered mesoporous carbon[25] were prepared and applied for the removal of pollutants such as hexavalent chromium, lead and phenol. Zhu and co-workers[26] have successfully prepared magnetic ordered mesoporous carbon as a catalyst support with superparamagnetic Fe–Pt nanoparticles without aggregation and particle growth. Zheng *et al.*[27] reported Pd supported on boron-doped mesoporous carbon as a highly active catalyst for liquid phase catalytic hydrodechlorination. Wang *et al.*[28] found Pd and Rh catalysts supported on N-doped mesoporous carbon having higher activities in the oxidation of benzyl alcohol than other carbon supports.

In addition to N and B, phosphorus (P) is expected to fit well into the carbon matrix because P-doping induces defects in the carbon framework and increases electron delocalization which promotes active sites.[29] Besides, phosphorus is similar to other heteroatoms (N, B, and S) when doping in carbon supports; it is also favorable for enhanced metal–support interaction between superficial metal clusters and substitutional heteroatom defects,[27,30,31] which may eventually affect the physicochemical properties of superficial metal particles such as their dispersion and composition. Therefore, it is hypothesized that Pd/Fe bimetallic nanoparticles embedded within innovative phosphorus-doped ordered mesoporous carbons would display a unique catalytic performance.

Herein, we employed a series of phosphorus-doped ordered mesoporous carbon (P-OMC) composites incorporated with reactive Fe and Pd bimetallic nanoparticles (Pd/NZVI@P) as effective and stable catalysts for the dechlorination of CPs in wastewater. Fe particles were *in situ* formed and incorporated in the P-OMC with uniform distribution, small size and large surface area to increase their mechanical activity and stability, and the noble metal Pd was applied to modify the Fe surface to facilitate electron generation for CP dechlorination. In this work, 2,4-dichlorophenol was selected as a model pollutant to evaluate the dechlorination activity. The effect of Pd loadings on the hydrodechlorination of 2,4-dichlorophenol was investigated. Moreover, it is known that the passivation of Fe-based materials significantly affects the dechlorination of CPs. Although some experimental parameters, such as solution temperature and initial substrate concentration as well as the reaction pathway of nanoscale Pd–Fe for dechlorination have been previously investigated in the literature,[8] the underlying mechanism for the passivation and the effect of solution pH on the passivation and activity have not yet been clearly elucidated. In this work, the effect of solution pH on the dechlorination and passivation of the Pd/NZVI@P was studied carefully, and the possible reasons were revealed.

Experimental

Chemicals and materials

Pluronic copolymer P123 ($EO_{20}PO_{70}EO_{20}$, EO = ethylene oxide, PO = propylene oxide) and triphenylphosphine (TPP) were purchased from Sigma-Aldrich (USA). All reagents were analytical grade and used as received without further purification. High-purity water (18.2 $M\Omega\ cm^{-1}$) from a Millipore Milli-Q water purification system was used in each experiment.

Synthesis of Pd/NZVI@P catalysts

The mesoporous template SBA-15 was prepared according to our previous study (as presented in the ESI†).[32–35] The preparation of P-OMC nanoparticles used conventional ordered mesoporous silica SBA-15 with a rodlike shape as a hard template. The carbon replica is then prepared by infiltrating the mesopores of 1000 mg of SBA-15 with 400 mg of triphenylphosphine (TPP) in 10 mL of ethyl alcohol at room temperature. Then, 2.0 mL of furfuryl alcohol was added dropwise into the above mixture. After that, the mixture thus prepared was heated at 80 °C for 10 h in air and calcined at 900 °C for 2 h under flowing nitrogen atmosphere. After dissolving the silica framework with 2.0 mol L^{-1} NaOH solution at 90 °C, the resultant solid was filtered, washed, dried and then stored in a nitrogen-filled glovebox until required. Details about the preparation of Pd/NZVI@P-0%, Pd/NZVI@P-0.5%, Pd/NZVI@P-1% and Pd/NZVI@P-2% are presented in the ESI.† For comparison, Pd/NZVI/OMC was also prepared by a similar method.

Characterization

Transmission electron microscopy (TEM, JEOL JEM-1230), high-resolution TEM (HR-TEM) at an accelerating voltage of 200 KV and scanning electron microscopy (SEM, JEOL JSM-6700) images were used to investigate the morphology and structure of Pd/NZVI@P. X-ray diffraction analysis (Rigaku D/max-II B) was applied to analyze the composite materials. Energy dispersive X-ray (EDX) analysis in the SEM image was applied to detect the element mapping of the Pd/NZVI@P. Nitrogen adsorption measurements at 77 K were performed using an ASAP 2020 volumetric adsorption analyzer. Raman spectroscopy was mounted by using a LabRam HR800 Raman spectrometer. Thermogravimetric-differential thermal analysis (DTG-DTA) was performed in order to determine the relevant phase transition temperatures. X-ray photoelectron spectroscopy (XPS, Thermo Fisher Scientific, UK) was performed to analyze the surface elemental composition.

Dechlorination experiments

All dechlorination experiments were carried out in 50 mL flasks containing 50 mg L^{-1} 2,4-DCP solution and a certain amount of Pd/NZVI@P, and the flasks were shaken at 150 rpm in a shaker at 25 °C. Before each experiment, 5 mg of Pd/NZVI@P-2% nanoparticles were added to a 2,4-DCP solution at an initial pH of 3.0, and the residual 2,4-DCP concentration was measured at 150 min. To compare the dechlorination of different CPs, 5 mg of Pd/NZVI@P-2% were placed in solutions of 2-CP, 4-CP, 2,4-DCP and 2,4,6-TCP at an initial pH of 3.0, and the reaction time was 150 min. To investigate the effect of initial pH on the dechlorination, 5 mg of Pd/NZVI@P-2% were added to 2,4-DCP solution at pH from 3.0 to 9.0 (pH was adjusted by adding dilute oxalic acid solution or aqueous ammonia), and 2,4-DCP concentration and pH in solution were measured during 150 min. All batch systems were carried out in conical flasks with ground-in glass stoppers, and the reaction solution was deoxygenated by inert gas. Each experiment was conducted in triplicate, and the standard deviations were calculated.

2,4-Dichlorophenol analysis

After the dechlorination experiments, the solid was separated from the solution by filtering with a 0.45 μm membrane filter, and the residual 2,4-DCP concentration in solution was measured by HPLC. The analytical parameters, the equation for percent dechlorination, and the pseudo-first-order kinetic model are described in the ESI.†

Results and discussion

Catalyst characterization

The formation of a highly ordered uniform pore distribution can be seen in the TEM images of SBA-15 and P-OMC in Fig. 1a and b, demonstrating that the resultant mesoporous materials possess well-ordered 2D hexagonal mesostructures. The TEM and SEM images of Pd/NZVI@P are presented in Fig. 1c and d, respectively. As seen in Fig. 1c, the black nanoparticles dispersed uniformly on the P-OMC were Pd/Fe bimetal nanoparticles, and the nanoparticles with an average diameter of about 15 nm were dispersed on the carbon matrix. The SEM image revealed that the mesoporous sample consisted of many rope-like domains with relatively uniform lengths, which were aggregated into wheat-like macrostructures (Fig. 1d). Pd/Fe bimetal nanoparticles particles dispersed on the P-OMC. In addition, as clearly observed in Fig. S-1 and S-2,† Pd/Fe bimetallic nanoparticles supported on OMC with P resulted in smaller and more highly dispersed particles compared to without P. Furthermore, SEM can give an elemental distribution map through images of backscattered electrons and EDS as well as surface topographic information through those of secondary electrons.[11,36] Fig. 2 shows SEM photographs and the corresponding EDS elemental mapping of Pd/NZVI@P-2%. The EDS elemental maps confirm that C, P, Fe and Pd elements are highly dispersed in Pd/NZVI@P. The relative atomic contents of these elements are listed in Table S-1.†

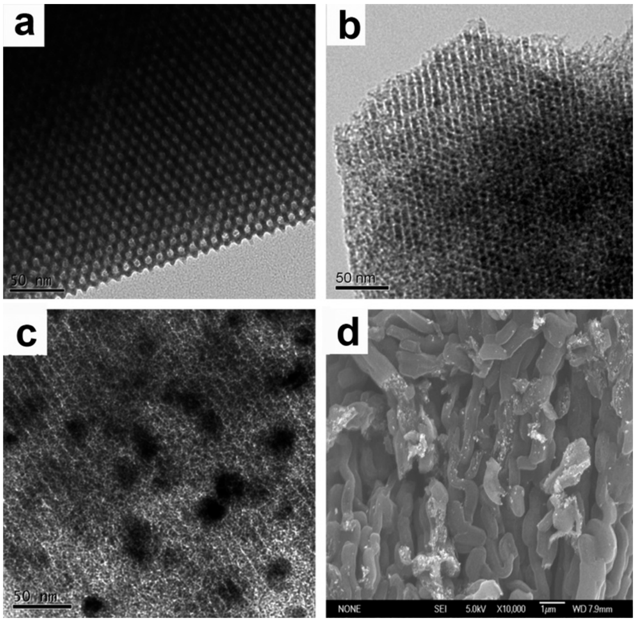

Fig. 1 TEM images of SBA-15 (a), P-OMC (b) and Pd/NZVI@P-2% (c). SEM of Pd/NZVI@P-2% (d).

The N_2 adsorption–desorption isotherms and Barrett–Joyner–Halenda (BJH) mesopore size distribution plots of

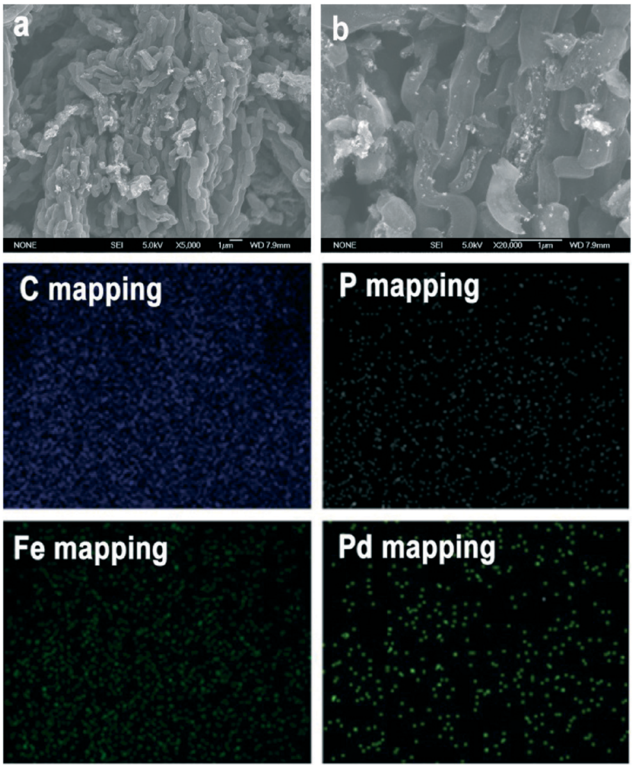

Fig. 2 SEM images of Pd/NZVI@P-2% at low (a) and high (b) magnifications, and elemental mapping images of Pd/NZVI@P-2% for C, P, Fe and Pd.

SBA-15, P-OMC, Pd/NZVI@P-0%, Pd/NZVI@P-0.5%, Pd/NZVI@P-1% and Pd/NZVI@P-2% are presented in Fig. 3. Their corresponding Brunauer–Emmett–Teller (BET) surface areas, pore volumes, and pore diameter are summarized in Table S-2.† All samples show representative type IV curves with H2 hysteresis loops (Fig. 3a), reflecting the uniform pore size distributions of the mesopores before and after P, Fe and Pd incorporation with SBA-15. The pore size distribution curves calculated from desorption branches clearly confirm their narrow pore size distribution. Compared with SBA-15, P-OMCs revealed a slight change in the H2 hysteresis loop, demonstrating that P was introduced into the carbon materials. The corresponding pore size distributions calculated from the adsorption branch clearly confirmed that (Fig. S3b†) the pore sizes of SBA-15 were centered at around 10 nm. In contrast, the adsorption pore size distribution of P-OMC was centered at 5 nm. The difference could be attributed either to the shrinkage of filled carbon phosphide polymeric material inside the pores of SBA-15 during the high temperature treatment of the mesoporous silica/carbon phosphide composite or to the partial filling of the CN matrix in the mesopores of SBA-15. The introduction of P led to a distinct increase in Brunauer–Emmett–Teller (BET) surface area (from 473.897 to 1033.5 $m^2\ g^{-1}$) and pore volume (from 1.134 to 1.446 $cm^3\ g^{-1}$). These might be due to P entering into channels and partially occupying the pore spaces. The BET surface area of P-OMC is 1033.5 $m^2 \cdot g^{-1}$. Interestingly, upon bulk doping of Fe and different amounts of Pd into P-OMC, the BET surface areas of Pd/NZVI@P-0% (only Fe doped into P-OMC), Pd/NZVI@P-0.5%, Pd/NZVI@P-1% and Pd/NZVI@P-2% are 667.746, 552.42, 455.53 and 344.22 $m^2\ g^{-1}$, respectively (Table S-2†). The mean pore sizes of Pd/NZVI@P-0%, Pd/NZVI@P-0.5%, Pd/NZVI@P-1% and Pd/NZVI@P-2% are 5.087, 5.058, 5.011 and 4.979 nm, respectively (Table S-2†). The specific surface areas and pore volumes of the samples obviously increased and decreased slightly after the introduction of Fe and Pd supports (Table S-2†), suggesting that some smaller Pd/Fe particles existed inside the pore framework which partially occupied the spaces of the pore canals. Compared with P-OMC, there is only a slight change in the mesoporous size of P-OMC with the Pd/Fe bimetal nanoparticles embedded, suggesting that the ordered mesostructure is still well preserved after immobilization of Fe and Pd, which are beneficial to the catalyst.

The small-angle X-ray diffraction (SAXRD) patterns of composite materials are presented in Fig. 4. Usually, SAXRD reveals whether the formation of an ordered mesostructure was changed during the preparation of materials. For the composite materials, the XRD patterns show three well-resolved peaks (the (100), (110) and (200) peaks) with a hexagonal mesopore arrangement at 2θ of about 0.89°, 1.55°, and 1.88°, which illustrates that the hexagonal framework ordering of an ordered mesoporous structure is basically retained in the process of material preparation and also indicates a high periodic order in the arrangement of symmetry cells, which is in agreement with the TEM observations (see Fig. 1). Besides, another phenomenon that should be noted is that the intensity of diffraction peaks of composites decreases slightly with the introduction of Fe and Pd into

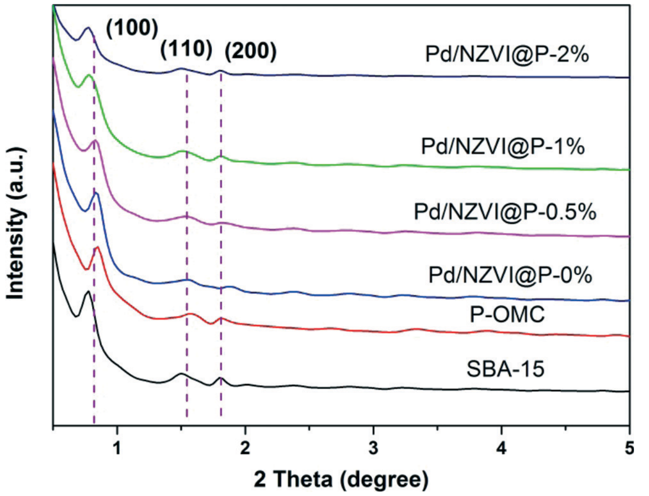

Fig. 4 Small-angle X-ray diffraction (SAXRD) patterns of nanocomposites.

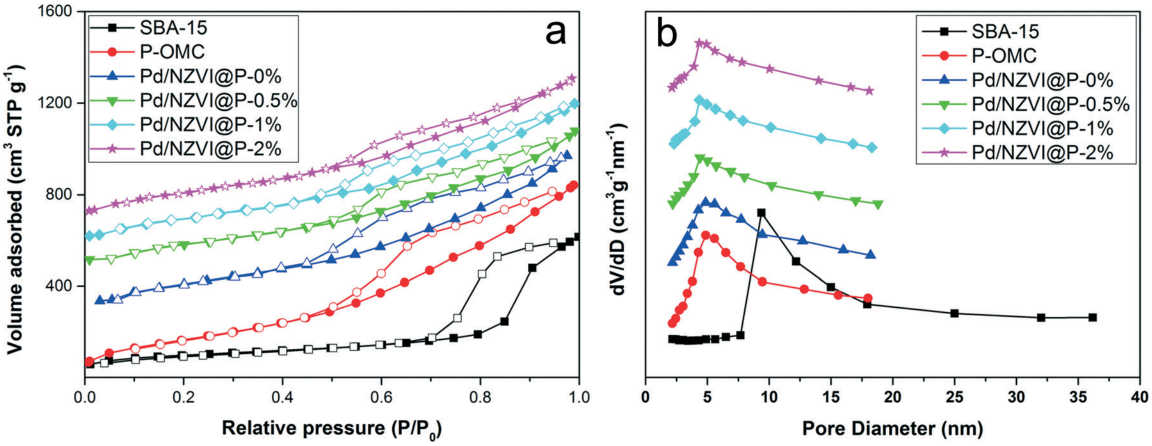

Fig. 3 Nitrogen sorption isotherms of nanocomposites (a) and the corresponding pore size distribution curves of composite materials (b).

P-OMC. These observations indicate that some of the Pd/Fe nanoparticles are located inside mesoporous carbon pores while some are located at the orifice of pores.

To elucidate the chemical composition, nature of bonding, and purity of the sample, the structural properties of the Pd/NZVI@P-2% particles were further investigated by XPS, and their spectra are shown in Fig. 5a–c. As seen in Fig. 5a, Pd/NZVI@P is mainly composed of carbon (C1s) and oxygen (O1s), with small amounts of phosphorus (P2p), iron (Fe 2p) and palladium (Pd3d). The presence of phosphorus comes from the pyrolyzation of triphenylphosphine, and iron and palladium mainly come from the reduction of $Fe(NO_3)_3 \cdot 9H_2O$ and palladium chloride inside the mesopores of P-OMC. Furthermore, the high-resolution P2p XPS spectrum (Fig. 5a inset) reveals the presence of both P–O bonding (134.03 eV) and P–C bonding (132.41 eV) in the Pd/NZVI@P catalyst. The two results strongly suggest that the P atoms are incorporated into the carbon framework of the P-OMCs. In addition, the peaks at 134.03 eV and 132.41 eV are positively shifted by 3.63 eV and 2.01 eV, respectively, compared with that of pure P (130.4 eV). The positive shift of the P2p peak indicates that there is a strong interaction between P, C and O.[37]

The Pd 3d regions of the particles are shown in Fig. 5b. For the Pd/NZVI@P-2%, the main doublet at 335.41 eV (Pd^0) and 336.48 eV (Pd^{2+}) are characteristic of metallic Pd, suggesting that both Pd^0 and Pd^{2+} coexist on the Pd/NZVI@P-2%, and the content of Pd^0 (68.22%) is larger than that of Pd^{2+} (61.78%). XPS analysis was also used to study the variation of the Fe oxidation state in resultant Pd/NZVI@P catalysts. As shown in Fig. 5c, the Fe 2p photoelectron spectrum of Pd/NZVI@P-2% showed four peaks around 725.11, 717.43, 712.36 and 706.26 eV in the $Fe2p_{1/2}$, satellite Fe^{3+}, $Fe2p_{3/2}$ and Fe^0, respectively, clearly indicating the Fe^0 species in the resultant Pd/NZVI@P catalysts. The results further confirm that Pd^0 and Fe^0 are incorporated into the carbon framework of the P-OMCs, which was also proved by previous SAXRD analysis.

Raman spectra illustrate the D-band and G-band of nanocomposites, giving some additional information about the carbon lattice. As seen in Fig. 5d, the nanocomposites possess both D mode and G mode peaks, which are near 1363 cm^{-1} and 1577 cm^{-1}, respectively. D mode corresponds to the disordered sp2-hybridized carbon atoms, while G mode is related to the structural integrity of sp2-hybridized carbon

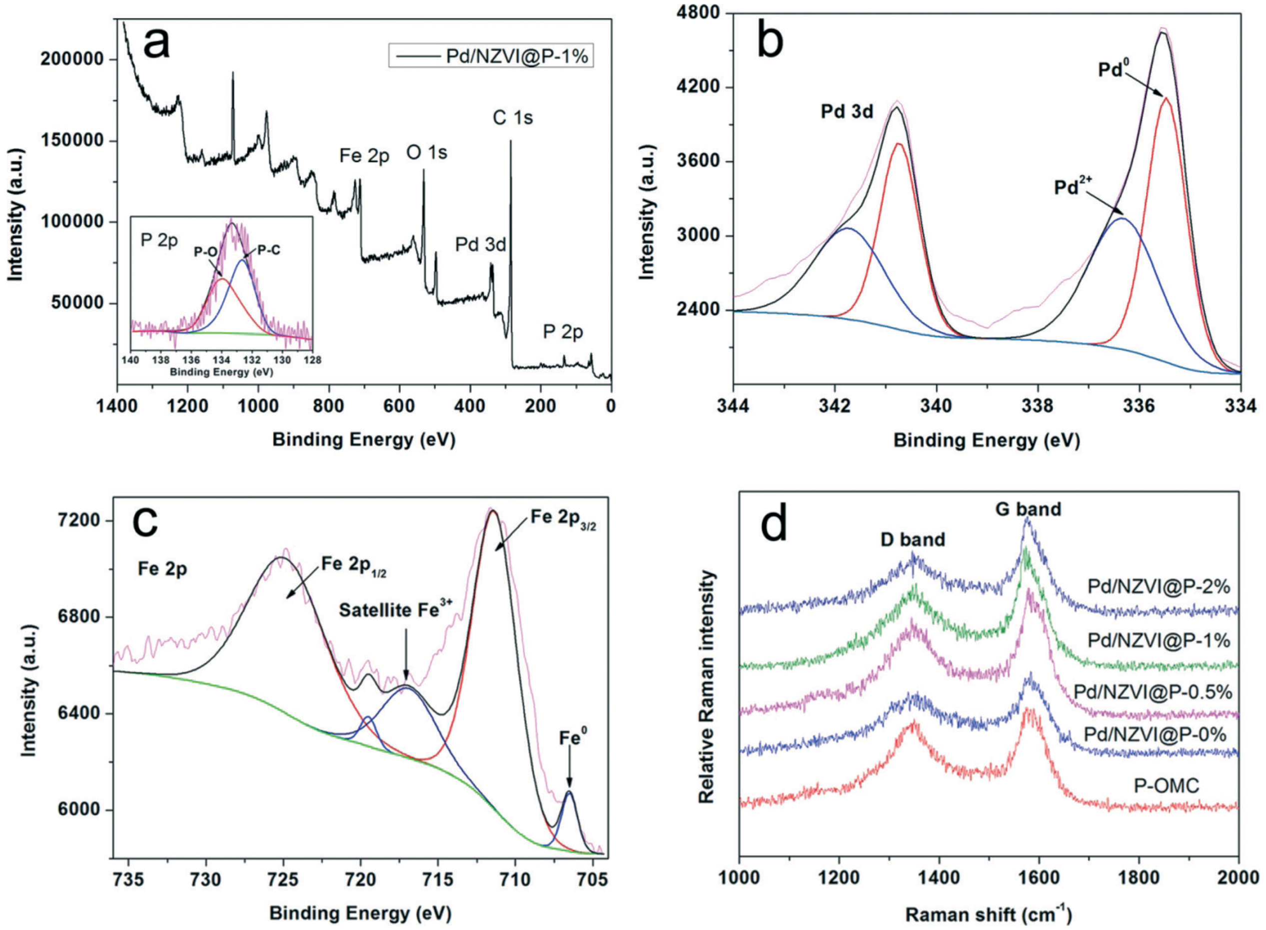

Fig. 5 XPS wide-scan spectrum of the Pd/NZVI@P-1% nanocatalyst (a) and the XPS spectra of the spent Pd 3d (b) and Fe 2p (c) catalyst, respectively. Raman spectra (d) of nanocomposites.

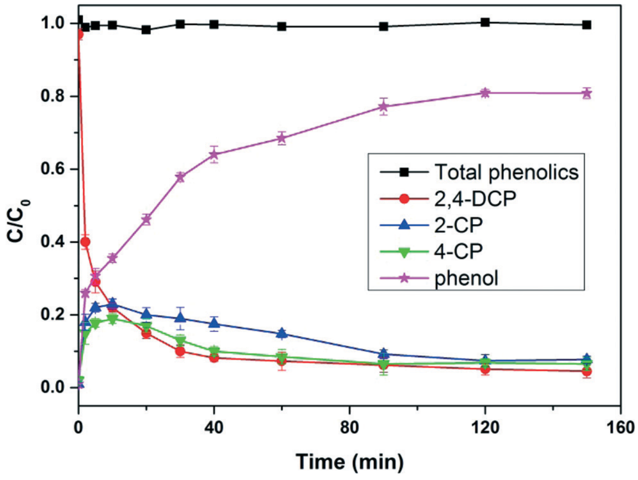

Fig. 6 Transformation of 2,4-dichlorophenol by 5 mg nanoscale Pd/NZVI@P-2%. C_0 = 50 mg L^{-1}, T = 25 °C, pH = 3.

atoms of ordered mesoporous carbons.[38] The ratio between the disorder and the graphite area bands (I_D/I_G) is interpreted as a measure of the degree of the material's orderliness and graphitization. As shown in Fig. 5d, the I_D/I_G ratios of P-OMC, Pd/NZVI@P-0%, Pd/NZVI@P-0.5%, Pd/NZVI@P-1% and Pd/NZVI@P-2% are 0.954, 0.922, 0.911, 0.901 and 0.894, respectively. The result indicates that the incorporation of Fe and Pd led to the small graphitization of Pd/NZVI@P. Besides, thermogravimetric-differential thermal analysis (DTG-DTA) was also used to characterize the catalysts (Fig. S-3†), and the description is presented in the ESI.†

Activity of Pd/NZVI@P on removal of 2,4-dichlorophenol

The dechlorination activity of the Pd/NZVI@P was investigated. As seen in Fig. 6, the concentration of 2-CP was higher than that of 4-CP in the reaction process, suggesting that the chlorine in the *para*-position is more easily expelled, which is in agreement with previous publications of other cases wherein dechlorination of chlorophenols by the catalytic reduction method began from the *para*-position of the ring.[39,40]

Interestingly, the phenol species could be detected as soon as the reaction occurred, and this phenomenon was also reported by Wei *et al.*[8] We assumed that the 2,4-DCP species were partly transformed into phenol directly prior to the appearance of transitional products. Moreover, it can be seen that the 2,4-DCP concentration decreased while 2-CP, 4-CP and phenol (P) concentrations increased with increasing reaction time to 150 min, and the total concentrations of phenolics (2,4-DCP, 2-CP, 4-CP and phenol) in solution were similar to the initial 2,4-DCP concentration, indicating that 2,4-DCP was directly reduced to 2,4-DCP, 2-CP, 4-CP and phenol in this process, and their amounts adsorbed on the bimetal were negligible. Given these observations, the hypothesis for the possible dechlorination processes is accordingly presented in Fig. 7.

During the catalytic hydrodechlorination of 2,4-dichlorophenol by Pd/NZVI@P, the factors including Pd content may have an important effect on the characteristics of Pd/NZVI@P and the dechlorination activity. Fig. 8 shows the dechlorination of 2,4-DCP on Pd/NZVI@P prepared with different amounts of Pd. The pseudo-first-order rate constants (K_{obs}) increased with increasing Pd content, similar to the trend of dechlorination efficiency. The Pd/NZVI@P with high Pd content displayed remarkable dechlorination activity, while the pure iron exhibited very poor dechlorination activity (Fig. 8). Pd/NZVI@P can form some galvanic cells, and Fe passed electrons to the catalytic Pd, which played important roles in both the acceleration of Fe corrosion and enhancement of dechlorination activity.[7] The low dechlorination efficiency over the pure Fe particles demonstrated that direct dechlorination of 2,4-DCP was difficult to occur without the assistance of Pd. The addition of Pd significantly improved the dechlorination of 2,4-DCP due to the mechanism of catalytic hydrodechlorination. Pd/NZVI@P-2% was adopted in the following experiments. The batch experimental results indicated that the 2,4-DCP species in aqueous solution were dechlorinated by Pd/NZVI@P-2%, followed by the formation

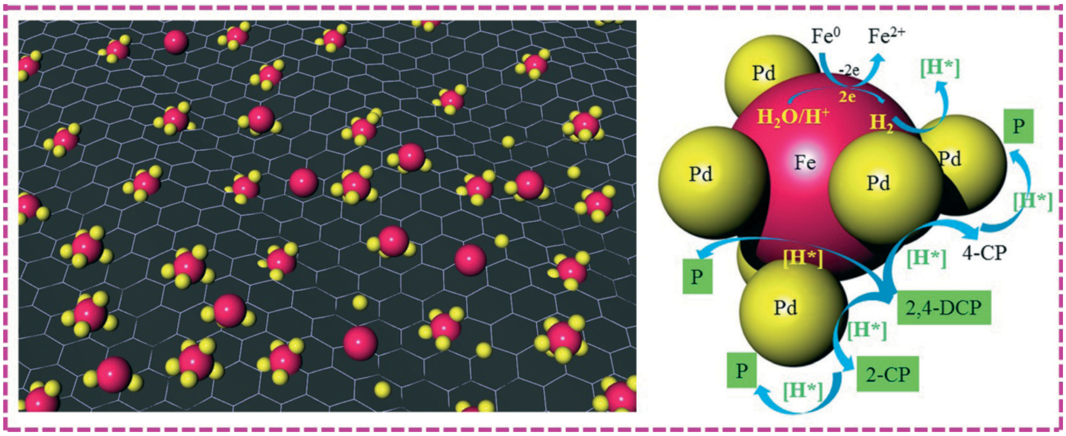

Fig. 7 The hypothesis for the possible dechlorination processes of 2,4-DCP.

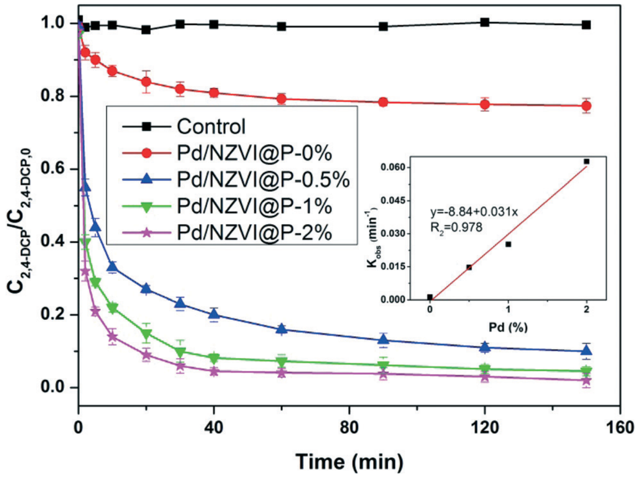

Fig. 8 Effect of Pd bulk loading on the removal ratio of 2,4-dichlorophenol.

and transformation of the intermediate products 2-CP and 4-CP and eventually of phenol as the final product. Besides, the dechlorination of 2,4-dichlorophenol by Pd/NZVI/OMC-2% and Pd/NZVI@P-2% was also compared, and the result is presented in Fig. S-4;† it is clear that P-OMC embedded with Pd/Fe bimetal nanoparticles is more suitable as a support for the dechlorination of 2,4-dichlorophenol, which is probably ascribed to the incorporation of heteroatoms (P).

Effect of pH on dechlorination and passivation

To investigate the effect of pH on the dechlorination and passivation of Pd/NZVI@P, the dechlorination of 2,4-DCP at different initial pH values was studied. As shown in Fig. 9, we found that the dechlorination efficiency of 2,4-DCP decreased when the initial pH increased from 3.0 to 6.0 (in acidic solution). However, when the initial pH was adjusted to 7.0, the dechlorination efficiency improved slightly and then decreased from 7.0 to 9.0 (in alkaline solution). Besides, it is clearly seen that the final pH increased when the initial pH increased from 3.0 to 8.0 during the dechlorination reaction. When the initial pH was 8.0, the final pH after the reaction was still around 8.0. However, the final pH decreased during the reaction when the initial pH was 9.0; these phenomena were also reported in other works.[8] Specifically, the pH variation profile in the reaction process was also investigated. The pH value during the dechlorination reaction increased rapidly within the initial 10 min, then gradually reached the highest value (as shown in Fig. S-3†), further decreased with increasing time, and finally kept relatively stable after 90 min. In the initial stage, Fe was dissolved in solution and 2,4-DCP was dechlorinated due to the following reactions:[8,41]

$$\text{(in acidic solution) } Fe^0 + 2H^+ \rightarrow Fe^{2+} + H_2 \tag{1}$$

$$\text{(in neutral or alkaline solution) } Fe^0 + 2H_2O \rightarrow Fe^{2+} + H_2 + OH^- \tag{2}$$

$$H_2 \xrightarrow{Pd} 2\left[H^*\right]_{abs} \tag{3}$$

$$2H^+ + 2e \xrightarrow{Pd} 2\left[H^*\right]_{abs} \tag{4}$$

$$RCl + [H^*] \rightarrow RH + Cl^- + H^+ \tag{5}$$

$$Fe^{2+} + 2OH^- \rightarrow Fe(OH)_2\ (K_{sp} = 4.87 \times 10^{-17}) \tag{6}$$

$$4Fe^{2+} + 2H_2O + O_2 \rightarrow 4Fe^{3+} + 4OH^- \tag{7}$$

$$3Fe^{3+} + 3OH^- \rightarrow Fe(OH)_3\ (K_{sp} = 2.79 \times 10^{-39}) \tag{8}$$

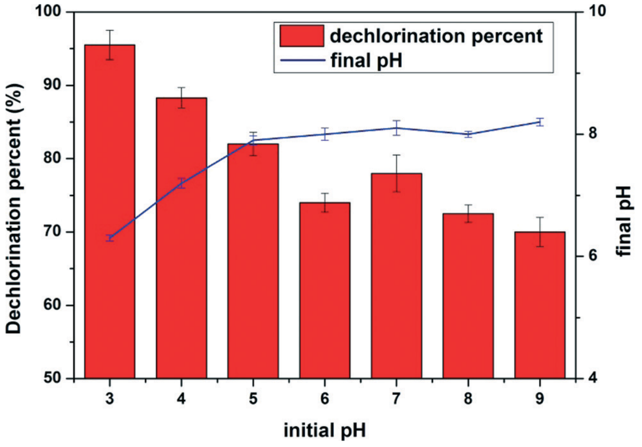

Fig. 9 Effect of initial pH and final pH on the dechlorination kinetics of 2,4-dichlorophenol.

These reactions caused the change in pH due to the consumption/formation of H^+ or consumption/formation of OH^-, making the solution pH change. As seen from eqn (6), the precipitation of $Fe(OH)_2$ occurred when the ion corrosion product of Fe^{2+} and OH^- was higher than the solubility product with the increase in Fe^{2+} and OH^- concentrations. In addition, $Fe(OH)_3$ can easily form, especially in the presence of dissolved oxygen (eqn (7) and (8)), although the solubility product of $Fe(OH)_3$ is much lower than that of $Fe(OH)_2$. In addition, the solution pH decreased due to the fast consumption of OH^- *via* the formation of iron hydroxide precipitate (eqn (6)–(8)).[42]

However, when the initial pH increased from 3.0 to 8.0, the precipitation rate was lower than the consumption rate of H^+ or generation rate of Fe^{2+}, and the solution pH still increased until the consumption rate of H^+ or generation rate of Fe^{2+} decreased to its precipitation rate or consumption rate of OH^-. When the initial pH was 8.0, the overall reaction equilibrium of the consumption of H^+ and OH^- was achieved at a relatively stable pH. Finally, when the initial pH was 9.0, the highest pH values exceeded 8.0 in the reaction process, accelerating the formation of passive film by iron hydroxide, resulting in the final pH decrease.

Besides, on the basis of the reaction mechanisms (eqn (1)–(8)), we could speculate that the main factors affecting dechlorination efficiency were as follows: (I) the generated rate of $[H]_{abs}$, which is related to the pH and the amount of Pd/NZVI@P (eqn (1)–(4)); (II) the passivation film by iron hydroxide, which could inhibit the contact of target compounds with the reactive sites and block the electron transfer; (III) the loss of Fe during reaction, resulting in the slow and even complete stop of the dechlorination reaction. In acidic solution, with the increase in H^+ concentration, the generated rate of $[H]_{abs}$ will increase quickly. Although the formation of passivating film is difficult due to the fact that the precipitation rate was lower than the consumption rate of H^+, excessive H^+ formation can remarkably result in the loss of Fe. However, the dechlorination efficiency of 2,4-DCP still increased quickly with the decrease in the initial pH (Fig. 9, the initial pH decreased from 6.0 to 3.0). The reason might be that despite the increase in H^+ resulted in the loss of Fe, the use of P-OMC as supporting material could provide enough Pd/Fe bimetal nanoparticles with high activity and stability, and the passivating film formed by iron hydroxide could be ignored. Thus, we speculate that the generated rate of $[H]_{abs}$ is the main influence on the dechlorination efficiency in acidic solution. In alkaline solution, the passivating film is formed easily, at initial pH beyond 7.0, the highest pH values exceeded 9.0 in the reaction process, accelerating the formation of passive film by precipitation. Some formed Fe (II) and Fe (III) precipitates covered the particle surface and retarded Fe dissolution (eqn (2)), resulting in slow dechlorination. Thus, with the increase in pH, the dechlorination efficiency decreased obviously. We speculate that the passivating film formed by iron hydroxide is the main limitation factor on dechlorination efficiency in alkaline solution. Moreover, it is clearly seen that alkaline solution is unfavorable for dechlorination compared with acidic solution. It is unexpected that the dechlorination efficiency improved slightly in neutral solution compared with the initial pH of 6.0. As described previously, the $[H]_{abs}$ at a pH of 6.0 is absolutely higher than that in neutral solution, which suppressed the formation of passivating film by iron hydroxide, which is conducive to the dechlorination. But the result is just the opposite. Interestingly, when the initial pH values were 6.0 and 7.0, after 150 min the final pH was similar (see Fig. S-5†), indicating that the rate of formation of OH^- was faster compared with the initial pH of 6.0. Thus, we speculate that the initial pH of 6.0 led to formation of more passivating film compared with that in neutral solution, and this might be the main factor that impacts dechlorination. In addition, the dissolved total iron ion and palladium ion concentrations at different pH values after Pd/NZVI@P reaction with 2,4-DCP in 150 min were also measured. As shown in Fig. S-6A,† after the reaction of Pd/NZVI@P with 2,4-DCP, the Pd/NZVI@P bimetal in acidic conditions releases iron ions because ZVI can react with H^+. The concentration of iron ions decreased with the increase in pH. However, there were nearly no palladium ions released at pH ranging from 3.0 to 9.0 because palladium just acted as the electronic conductor. As seen in Fig. S-6B,† there was nearly no P released at pH ranging from 3.0 to 9.0 after the reaction; the reason may be that P is not directly involved in the dechlorination of 2,4-dichlorophenol.

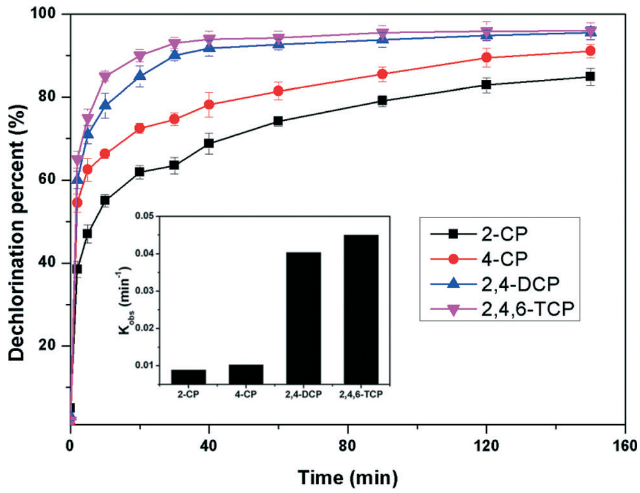

Fig. 10 The dechlorination activity of Pd/NZVI@P-2% for different CPs (5 mg nanoscale Pd/NZVI@P-2%, C_0 = 50 mg L^{-1}, T = 25 °C, pH = 3).

In general, solution pH not only affects the dechlorination of 2,4-DCP but also influences the formation of iron hydroxide precipitate and the passivation. Low pH can cause fast dechlorination but result in dissolution of bimetal. The increasing pH accelerated the formation of iron precipitates, and passivating film was formed. Therefore, it is crucial to control the solution pH in a reasonable range to balance the dechlorination and passivation of bimetal.

Effect of the number and position of chlorine atoms of CPs on the dechlorination activity

In addition, we preliminarily discussed the number and position of chlorine atoms on CPs for the dechlorination activity of the Pd/NZVI@P. In this study, 2-CP, 4-CP, 2,4-DCP and 2,4,6-trichlorophenol (2,4,6-TCP) were used as the substrates. As shown in Fig. 10, the K_{obs} of different CPs follows the order of 2,4,6-TCP > 2,4-DCP > 4-CP >2-CP, and the dechlorination efficiency obeys the same order as that of K_{obs} during the dechlorination reaction (0–150 min). The result further implies that the dechlorination of CPs by chemical reactions preferentially begin from the *para*-position of the ring (K_{obs} (4-CP) > K_{obs} (2-CP)), and more chlorine atoms of CPs are favorable for the C–Cl bond cleavage reaction to take place. This phenomenon was also reported in other works.[38,39,43]

Conclusions

The Pd/Fe bimetal nanoparticles embedded within phosphorus-doped ordered mesoporous carbons (Pd/NZVI@P) had high catalytic dechlorination activity for 2,4-DCP. In acidic, neutral or alkaline solution conditions, Pd/NZVI@P can completely remove 2,4-DCP from wastewater. Besides, the main factors affecting dechlorination efficiency related to solution pH were revealed. The high and stable dechlorination of 2,4-DCP was attributed to the homogeneous distribution of Pd/Fe bimetal nanoparticles into the phosphorus-doped ordered mesoporous carbons phase. This study demonstrated that P-OMC is a promising supporting material to prepare some effective composite metals for the catalytic dechlorination of CPs. Many bimetallic materials may also be supported by P-OMC with great prospects for wastewater treatment to dechlorinate CPs.

Acknowledgements

The study was financially supported by the National Program for Support of Top-Notch Young Professionals of China (2012), Projects 51222805, 51579096, 51521006 and 51508175 supported by National Natural Science Foundation of China, the Program for New Century Excellent Talents in University from the Ministry of Education of China (NCET–11–0129), Interdisciplinary Research Project of Hunan University, the Fundamental Research Funds for the Central Universities, Hunan University, and the Hunan Province Innovation Foundation for Postgraduate (no. CX2015B095).

References

1 J. Xu, Q. Jiang, T. Chen, F. Wu and Y. X. Li, *Catal. Sci. Technol.*, 2015, **5**, 1504–1513.

2 L. Yin, Z. Shen, J. Niu, J. Chen and Y. Duan, *Environ. Sci. Technol.*, 2010, **44**, 9117–9122.

3 S. Agarwal, S. R. Al-Abed and D. D. Dionysiou, *Environ. Sci. Technol.*, 2007, **41**, 3722–3727.

4 U. D. Patel and S. Suresh, *J. Hazard. Mater.*, 2008, **156**, 308–316.

5 Y. Weile, A. A. Herzing, L. X. Qin, C. J. Kiely and Z. W. Xian, *Environ. Sci. Technol.*, 2010, **44**, 4288–4294.

6 R. Devor, K. Carvalho-Knighton, B. Aitken, P. Maloney, E. Holland, L. Talalaj, R. Fidler, S. Elsheimer, C. A. Clausen and C. L. Geiger, *Chemosphere*, 2009, **76**, 761–766.

7 F. Xu, S. Deng, J. Xu, W. Zhang, M. Wu, B. Wang, J. Huang and G. Yu, *Environ. Sci. Technol.*, 2012, **46**, 4576–4582.

8 J. Wei, X. Xu, Y. Liu and D. Wang, *Water Res.*, 2006, **40**, 348–354.

9 R. G. Luthy, G. R. Aiken, M. L. Brusseau, S. D. Cunningham, P. M. Gschwend, J. J. Pignatello, M. Reinhard, S. J. Traina, W. J. Weber and J. C. Westall, *Environ. Sci. Technol.*, 1997, **31**, 3341–3347.

10 N. Saleh, K. Sirk, Y. Liu, T. Phenrat, B. Dufour, K. Matyjaszewski, R. D. Tilton and G. V. Lowry, *Environ. Eng. Sci.*, 2007, **24**, 45–57.

11 Y. Wang, H. Zhao and G. Zhao, *Appl. Catal., B*, 2015, **164**, 396–406.

12 M. Zhang, D. B. Bacik, C. B. Roberts and D. Zhao, *Water Res.*, 2013, **47**, 3706–3715.

13 S. Navalon, M. Alvaro and H. Garcia, *Appl. Catal., B*, 2010, **99**, 1–26.

14 M. Hartmann, S. Kullmann and H. Keller, *J. Mater. Chem.*, 2010, **20**, 9002–9017.

15 S. Navalon, A. Dhakshinamoorthy, M. Alvaro and H. Garcia, *ChemSusChem*, 2011, **4**, 1712–1730.

16 C. Z. Yuan, L. Chen, B. Gao, L. H. Su and Q. X. Zhang, *J. Mater. Chem.*, 2009, **19**, 246–252.

17 R. Ryoo, H. J. Sang and S. Jun, *J. Phys. Chem. B*, 1999, **37**, 7743–7746.

18 F. B. Su, Z. Q. Tian, C. K. Poh, Z. Wang, S. H. Lim and Z. L. Liu, *Chem. Mater.*, 2010, **22**, 832.

19 G. Gupta, D. A. Slanac, P. Kumar, J. D. Wiggins-Camacho, X. Wang, S. Swinnea, K. L. More, S. Dai, K. J. Stevenson and K. P. Johnston, *Chem. Mater.*, 2009, **21**, 4515–4526.

20 Z. Li, J. Liu, Z. Huang, Y. Yang, C. Xia and F. Li, *ACS Catal.*, 2013, **3**, 839–845.

21 Z. Liu, F. Su, X. Zhang and S. W. Tay, *ACS Appl. Mater. Interfaces*, 2011, **3**, 3824–3830.

22 J. S. Yu, S. Kang, S. B. Yoon and G. Chai, *J. Am. Chem. Soc.*, 2002, **124**, 9382–9383.

23 G. Yang, L. Tang, Y. Cai, G. Zeng, P. Guo, G. Chen, Y. Zhou, J. Tang, J. Chen and W. Xiong, *RSC Adv.*, 2014, **4**, 58362–58371.

24 T. Lin, G. D. Yang, G. M. Zeng, C. Ye, S. S. Li, Y. Y. Zhou, Y. Pang, Y. Y. Liu and Y. Zhang, *Chem. Eng. J.*, 2014, **239**, 114–122.

25 G. Yang, T. Lin, G. Zeng, C. Ye, T. Jing, Y. Pang, Y. Zhou, Y. Liu, J. Wang and S. Zhang, *Chem. Eng. J.*, 2015, **259**, 854–864.

26 Y. Zhu, E. Kockrick, S. Kaskel, T. Ikoma and N. Hanagata, *J. Phys. Chem. C*, 2009, **113**, 5998–6002.

27 J. Zhou, W. Ke, W. Wang, Z. Xu, H. Wan and S. Zheng, *Appl. Catal., A*, 2014, **470**, 336–343.

28 B. Wang, M. Lin, T. P. Ang, J. Chang, Y. H. Yang and A. Borgna, *Catal. Commun.*, 2012, **25**, 96–101.

29 D. S. Yang, D. Bhattacharjya, S. Inamdar, J. Park and J. S. Yu, *J. Am. Chem. Soc.*, 2012, **134**, 16127–16130.

30 C. K. Acharya and C. H. Turner, *J. Phys. Chem. B*, 2006, **110**, 17706–17710.

31 C. K. Acharya and C. H. Turner, *J. Phys. Chem. C*, 2007, **111**, 14804–14812.

32 L. Tang, Y. Zhou, G. Zeng, Z. Li, Y. Liu, Y. Zhang, G. Chen, G. Yang, X. Lei and M. Wu, *Analyst*, 2013, **138**, 3552–3560.

33 Y. Zhou, L. Tang, G. Zeng, J. Chen, J. Wang, C. Fan, G. Yang, Y. Zhang and X. Xie, *Biosens. Bioelectron.*, 2015, **65**, 382–389.

34 Y. Zhou, L. Tang, G. Zeng, J. Chen, Y. Cai, Y. Zhang, G. Yang, Y. Liu, C. Zhang and W. Tang, *Biosens. Bioelectron.*, 2014, **61**, 519–525.35.

35 J. X. Liu, W. J. Zhou, J. L. Gong, L. Tang, Y. Zhang, H. Y. Yu, B. Wang, X. M. Xu and G. M. Zeng, *Bioresour. Technol.*, 2008, **18**, 8748–8751.

36 S. Wang, Q. Zhao, H. Wei, J. Q. Wang, M. Cho, H. S. Cho, O. Terasaki and Y. Wan, *J. Am. Chem. Soc.*, 2013, **135**, 11849–11860.
37 L. X. Ding, A. L. Wang, G. R. Li, Z. Q. Liu, W. X. Zhao, C. Y. Su and Y. X. Tong, *J. Am. Chem. Soc.*, 2012, **134**, 5730–5733.
38 S. Shrestha, S. Asheghi, J. Timbro and W. E. Mustain, *Carbon*, 2013, **60**, 28–40.
39 K. C. Christoforidis, M. Louloudi and Y. Deligiannakis, *Appl. Catal., B*, 2010, **95**, 297–302.
40 G. Díaz-Díaz, M. Celis-García, M. C. Blanco-López, M. J. Lobo-Castañón, A. J. Miranda-Ordieres and P. Tuñón-Blanco, *Appl. Catal., B*, 2010, **96**, 51–56.
41 X. Wang, M. Zhu, H. Liu, J. Ma and F. Li, *Sci. Total Environ.*, 2013, **449**, 157–167.
42 C. C. Liu, D. H. Tseng and C. Wang, *J. Hazard. Mater.*, 2006, **136**, 706–713.
43 S. Agarwal, S. R. Al-Abed, D. D. Dionysiou and E. Graybill, *Environ. Sci. Technol.*, 2008, **43**, 915–921.